A&A 380, 704–713 (2001)
DOI: 10.1051/0004-6361:20011251
© ESO 2001

Astronomy & Astrophysics

Two-dimensional multi-parameter fields of a limb flare loop system

X. M. Gu[1,2], J. P. Dun[1], and S. H. Zhong[1]

[1] Yunnan Observatory, CAS, Kunming 650011 and National Astronomical Observatories, CAS, Beijing 100012, PR China
[2] United Laboratory of Optical Astronomy, CAS, Shanghai 200030, PR China

Received 20 November 2000 / Accepted 7 August 2001

Abstract. The 2D H_β spectral data of the post-flare loop system (PFLs) of August 17, 1989 are obtained and analyzed quantitatively. Four physical parameters (the line-of-sight velocity $V_{//}$, column number density of the hydrogen atoms at the second level along the line-of-sight direction N_2, the excitation temperature $T_{\rm ex}$ and the micro-turblence velocity $V_{\rm t}$) and their 2D distributions are derived. The 2D fields of $V_{//}$, N_2, $T_{\rm ex}$ and $V_{\rm t}$ exhibit inhomogeneous and asymmetric properties in two loop legs. Red-shift velocities in the south leg are smaller than those of blue shift in the north leg where the velocity reaches 60 km s^{-1}. The values of N_2 and $T_{\rm ex}$ in the south leg are all much higher than those in the north leg, N_2 ranges between 0.5 to 4.5×10^{13} cm^{-2}, while $T_{\rm ex}$ ranges from 0.8 to 2.2×10^4 K, lower at the top part than in the two legs. A high temperature region is located in the middle of the south leg. $V_{\rm t}$ at the top part is greater than that in the two legs, with the average being 30∼40 km s^{-1}. Electron density $n_{\rm e}$ and electron pressure $P_{\rm e}$ are estimated at $0.2\sim0.6\times10^{11}$ cm^{-3} and at 0.04∼0.12 dyn cm^{-2}, respectively. These results are compared with those obtained from the PFLs of 1984 February 18.

Key words. Sun: flares – Sun: fundamental parameters

1. Introduction

The study of solar flares is an important and attractive topic in solar physics. Modern observations obtained from space and the ground show that solar flares have loop-like structures (Pneuman 1981). In general, flares are composed of more than one loop comprising a loop system. There are two kinds of loops: X-ray loops and post-flare loops, the former ones are the hot (∼10^6 K) and high (∼10^5 km) loops observed with X-ray telescopes on space satellites; the latter ones are the cool (∼10^4 K) and low (∼10^4 km) loops observed in the H_α line. The relationship between the hot X-ray and cool H_α post-flare loops observed on June 26, 1992, was well studied by Schmieder et al. (1995, 1996a) and their evolution was also given (Schmieder et al. 1996b).

In order to explain the formation mechanism of the cool and hot loops, a model of magnetic field lines which are attached to the photosphere, extending into the corona and continuously reconnecting to form magnetic loops at the base of the corona was proposed by Sturrock (1968), and later by Kopp & Pneuman (1976). Although the model successfully explained the upward motion of material at the reconnection site, it did not account for the large downward mass flow observed in the legs of the cool loops. Forbes & Malherbe (1986) introduced a fast-mode shock into the model and studied a complete MHD reconnection model, which could explain not only the downward mass flow, but also the material replenishment of the loop by chromospheric ablation. Based on the improved model, Forbes et al. (1989) evaluated the relationship between the physical parameters of the hot and cool plasma loops.

A 2D spectroscopic study is necessary to explore the physical structure and dynamical evolution properties of a whole post-flare loop system. By spectral analysis, one may determine quantitatively many physical quantities of flares (such as the velocity, density, temperature and pressure, etc.) which may be used to produce a model of solar atmospheric structure.

There are more difficulties in obtaining 2D spectral data of flares with a spectrograph than getting their H_α filtergrams with a telescope. So far, complete 2D multi-line spectroscopic data of solar flares have still been rare and the study of 2D multi-parameter fields of flares is very poor. Li et al. (1993) studied the limb flare loop system of 1984 February 18 and the 2D multi-parameter fields were

Send offprint requests to: Xiao Ma Gu,
e-mail: ssg@public.km.yn.cn

Article published by EDP Sciences and available at http://www.aanda.org or
http://dx.doi.org/10.1051/0004-6361:20011251

given in the H_α line. On the 17th of August 1989, another limb flare loop system was observed in the H_β line at the Yunnan Observatory with the same instrument. In this paper, four 2D parameter fields from the H_β spectral data of the flare observed on 1989 August 17 are given and the results obtained are compared with those derived from the flare of 1984 February 18.

2. Observations and data reduction

A large post-flare loop system (PFLs) which occurred above the big active region (NOAA 5629, S15°;W109°) on the solar western limb on August 17, 1989, was observed at the Yunnan Observatory with a two-dimensional MW-SSHG (multi-waveband spectra-spectroheliograph) instrument which is equipped with an H_α slit-jaw monitor (Xuan & Lin 1993). According to the *Solar Geophysical Data*, an X2.9 X-ray storm and a radio burst of 5600 flux units at 10 cm were accompanied by the PFLs, which appeared at 01:04 UT, reached its maximum at 02:40 UT and ended after 09:11 UT. It was characterized by the formation of some big flaring loops above the solar limb and forming a loop system with the loop planes almost facing on to the observer (i.e. the angle between the normal line of the loop plane and the line of sight is small). From 01:40 UT on, the loop system was observed with an H_α filter telescope and the MW-SSHG, which recorded 2D spectra of the flare in two lines by using a scanning technique with a step distance of $6''$. The spectra of H_α and H_β at four different times (02:35–02:40 UT; 03:14–03:18 UT; 03:41–03:45 UT; 06:36–06:40 UT) and the corresponding H_α images from the slit-jaw monitor were obtained simultaneously. Figures 1a and b give the H_α filtergrams and the H_β spectral frames, respectively. The PFLs was also observed with the solar vector-magnetograph equipped with an H_β filter at the Huairou Solar Station of the Beijing Astronomical Observatory (Li 1990). The H_β filtergrams at different time are given in Fig. 1c. This shows that the PFLs is composed of many sub-loops which have different heights and brightnesses between the two legs.

All spectral data are recorded on the film. Unfortunately, the H_α spectral data are over-exposured and cannot be used for photometric measurements, but the H_β-SSHG data taken in the prior three time intervals are well recorded. The data were measured with the PDS microdensitometer at the Purple Mountain Observatory, by using measurement steps along the slit and the dispersion directions being $4''$ and 25 μ ($\sim$0.02 Å), respectively. A great number of intensity profiles of H_β were obtained at different points of the PFLs after transforming from density to intensity and correcting for scattered light. Relative intensities of H_β profiles are transferred into the absolute ones by use of the calibrated spectra taken at the centre of solar disk where there is no sunspot group. There are 201 profiles in nine spectral frames computed in the paper, most of them are multi-peak and asymmetric. Some of the typical H_β intensity profiles are given in Figs. 2a–e.

3. Method of data analysis

The spectral analysis method is a key problem. The profiles of solar flares are usually asymmetric, sometimes extremely asymmetric (see Figs. 2b–e). Hence, it is difficult to explain or process these asymmetric profiles. To solve this problem, a method of "multi-cloud model" (MCM) is proposed by Gu et al. (1996). In general, this method enables us to explain and deal with the asymmetric profiles of flares which occur on the solar disk or at the limb.

3.1. Principle

It is considered that a non-Gaussian profile is the sum of several (for example, m) Gaussian sub-profiles produced by m small emitting elements (the so-called "clouds") which show different or identical physical properties. On the other hand, based on the research of profile asymmetry in prominences made by Ye et al. (1985) and Chen et al. (1987) by means of numerical and analytical methods, respectively, it is concluded that a main reason why an asymmetric profile is produced in a prominence spectrum is that the source function and the velocity field within the prominence exhibit a non-linear variation with depth simultaneously. Therefore, we can use this analogy to describe a non-linear change by use of some small emission elements (i.e. "clouds"), which are aligned along the line-of-sight direction, with different (or identical) properties within the solar atmosphere and where there are different source functions and velocities. The sketch of the model is given in Fig. 3. For simplicity, the S and V in each "cloud" are assumed to be constants, with each cloud being not optically thick, and the profile is only broadened due to the Doppler effect. For the objects at the solar limb, the total intensity emitted by the m "clouds" I_λ should be

$$I_\lambda = \sum_{j=1}^{m} S_j(1 - \mathrm{e}^{-\tau_{\lambda,j}})\exp(-\sum_{i=0}^{j-1}\tau_{\lambda,i}), \tag{1}$$

where, m is the number of the "cloud" or the sub-profile. Given $\tau_{\lambda,0} = 0$, the optical depth of the jth emission element is written as

$$\tau_{\lambda,j} = \tau_{0,j}\exp\left[-\left(\frac{\Delta\lambda - \Delta\lambda_{0,j}}{\Delta\lambda_{\mathrm{D},j}}\right)^2\right]. \tag{2}$$

In Eqs. (1) and (2) S_j, $\tau_{0,j}$, $\Delta\lambda_{0,j} = \lambda_0 V_{//,j}/\mathrm{c}$ and $\Delta\lambda_{\mathrm{D},j}$ are the source function, optical depth at the line centre, Doppler shift and Doppler width of the jth "cloud", respectively.

3.2. Mathematical analysis

In general, for a limb PFLs, the intensity value of a spectral profile at a point with wavelength λ_j can be written as

$$I_{\lambda_j} = F(\lambda_j, \boldsymbol{X}), \tag{3}$$

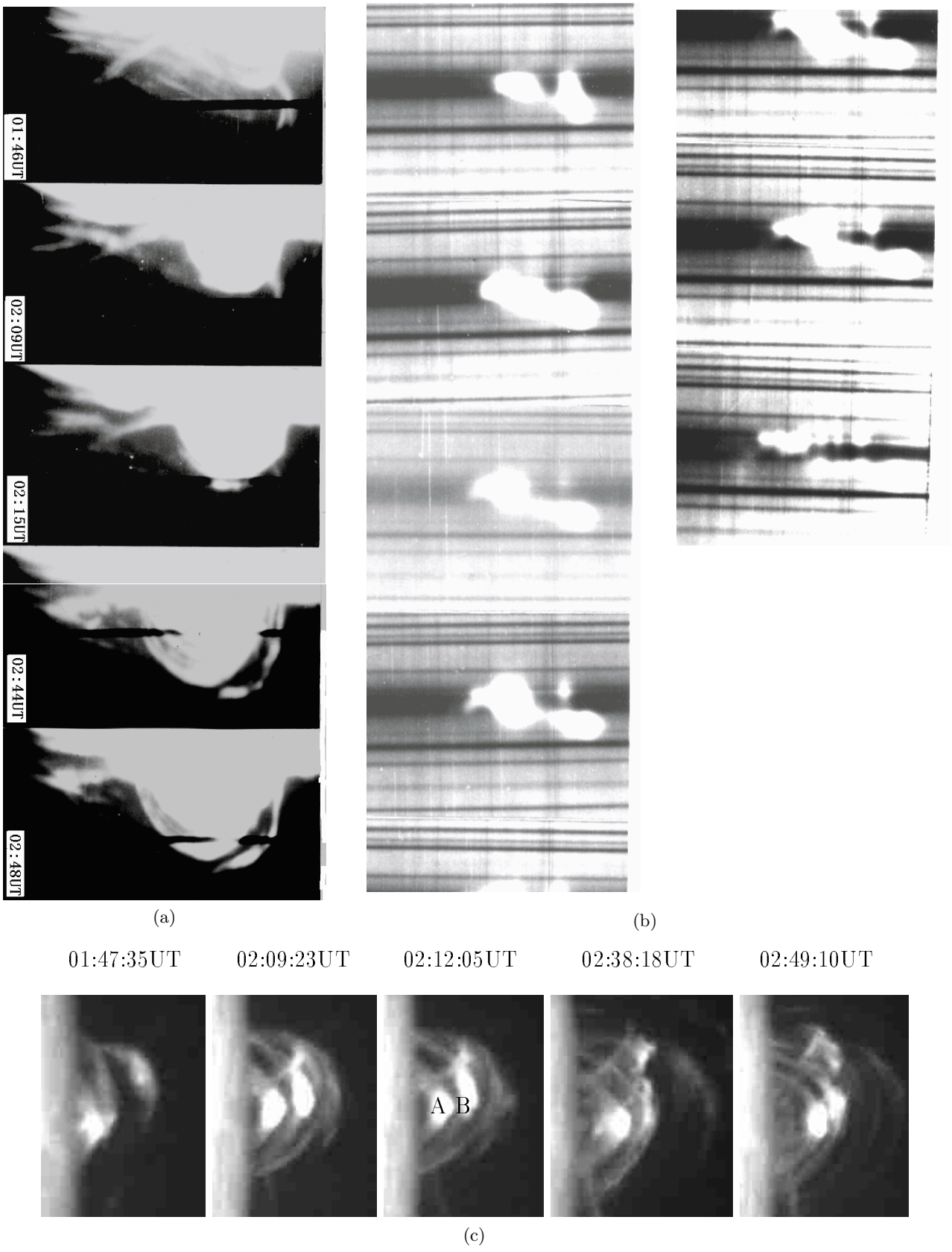

Fig. 1. Post-flare loop system of 1989 August 17 observed with the MW-SSHG at the Yunnan Observatory. **a)** H_α filtergrams with slit-jaw monitor taken in different time. The black lines in the pictures show the positions of the incident slit of the spectroheliograph. The north is up, and west is to the right. The scan is carried out from the top of loops to the solar limb. **b)** A part of the synchronous spectral scan pictures in H_β line taken from 02:35 UT to 02:40 UT. From the left to the right a series of scanning frames are shown and the decrease in wavelengths is given for each spectral frame. **c)** H_β filtergrams taken with the Solar Vector Magnetograph at the Huairou Solar Station of the Beijing Astronomical Observatory.

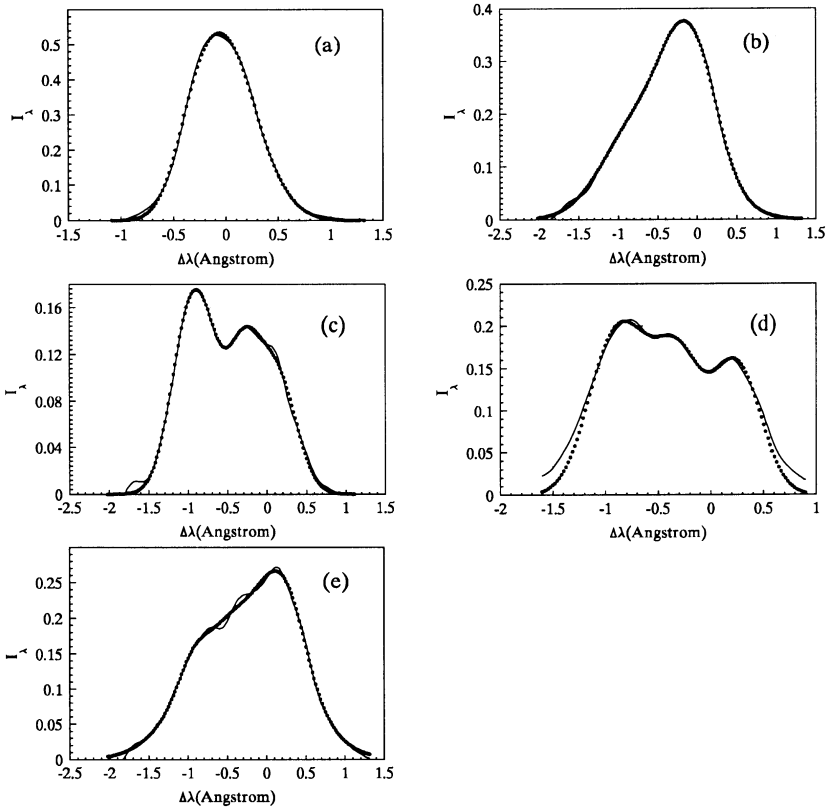

Fig. 2. The H_β profiles of the flare on 1989 August 17. The solid lines refer to the observed profiles, and the dotted lines refer to the theoretical profiles computed by means of the multi-cloud model method. **a)** Corresponds to $m = 1$, and **b) c)** and **d) e)** to $m = 2$ and 3, respectively.

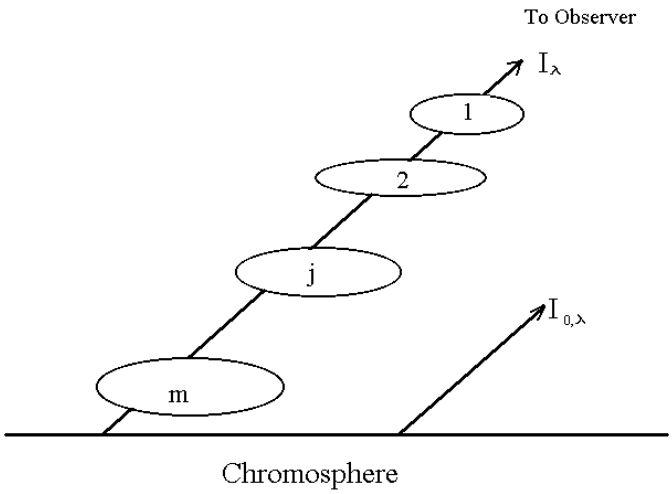

Fig. 3. A scheme of the multi-cloud model, where $I_{0,\lambda}$ is the background radiation of the chromosphere and I_λ the observed intensity.

where, $\boldsymbol{X} = (x_1, x_2, \ldots, x_{4m})$ and $x_1, x_2, \ldots, x_{4m}$ are $4m$ independent physical parameters. According to the least square method, the best representation of the total intensity $I^{\rm obs}_{\lambda_j}$ observed at the jth wavelength point is obtained when

$$\psi(\boldsymbol{X}) = \sum_{j=1}^{n} [F(\lambda_j, \boldsymbol{X}) - I^{\rm obs}_{\lambda_j}]^2 \tag{4}$$

is a minimum, where, n is the total number of wavelength points measured ($n > m$). The vector that minimizes $\psi(\boldsymbol{X})$ must satisfy the following equation:

$$\frac{\partial \psi(\boldsymbol{X})}{\partial X_k} = 2 \sum_{j=1}^{n} [F(\lambda_j, \boldsymbol{X}) - I^{\rm obs}_{\lambda_j}] \frac{\partial F_j}{\partial X_k} = 0, \tag{5}$$

where $F_j = F(\lambda_j, \boldsymbol{X})$, $k = 1, 2, \ldots, 4m$. In general, Eq. (5) is non-linear and can be solved by using a complete linearization method (Fang 1985). Assuming that $\boldsymbol{X_0}$ is an approximate solution and $\boldsymbol{X} = \boldsymbol{X_0} + \delta \boldsymbol{X}$, we have

$$\phi_k(\boldsymbol{X_0} + \delta \boldsymbol{X}) = \frac{\partial \psi(\boldsymbol{X_0} + \delta \boldsymbol{X})}{\partial \boldsymbol{X_k}} = 0, \tag{6}$$

where $k = 1, 2, \ldots, 4m$. Expanding $\phi_k(\boldsymbol{X_0} + \delta \boldsymbol{X})$ into the Taylor series in the neighbourhood of $\boldsymbol{X_0}$ and neglecting the infinitesimal item of $\delta \boldsymbol{X}^2$ and higher orders, one may obtain the linearized equation

$$\sum_{i=1}^{4m} \sum_{j=1}^{n} \left\{ \left[F_j(\boldsymbol{X}) - I^{\rm obs}_{\lambda_j} \right] \frac{\partial^2 F_j}{\partial X_k \partial X_i} + \frac{\partial F_j}{\partial X_i} \frac{\partial F_j}{\partial X_k} \right\} \delta X_i + \phi_k(\boldsymbol{X_0}) = 0, \tag{7}$$

(where $k = 1, 2, \ldots, 4m$, $(4m < n)$) which can be solved iteratively. Equation (7) can be expressed as

$$\boldsymbol{A} \bullet \delta\boldsymbol{X} = \boldsymbol{B}, \tag{8}$$

where $\boldsymbol{A}$ is a $4m \times 4m$ matrix, $\boldsymbol{B}$ is a vector of $4m$ elements and $\delta\boldsymbol{X}$=$(\delta X_1, \delta X_2, \ldots, \delta X_{4m})$. From Eq. (8) one can obtain

$$\delta\boldsymbol{X} = \boldsymbol{A}^{-1} \bullet \boldsymbol{B}. \tag{9}$$

Therefore, $\boldsymbol{X} = \boldsymbol{X}_0 + \delta\boldsymbol{X}$. Taking $\boldsymbol{X}$ as $\boldsymbol{X_0}$ and substituting it into Eq. (8), you may find a new $\delta\boldsymbol{X}$ in the same way and so on until the $\delta\boldsymbol{X} \to 0$. Because the convergence is proportional to $(\delta X/X)^2$, the convergence is fast.

The solution is not mathematically unique, but one may select the one with physically reasonable values for the parameters that is consistent with the continuity assumption along the loops (Gu et al. 1992).

3.3. Application of the method

In Eq. (1), m is taken as 1, 2 and 3, corresponding to "one-cloud" (Beckers 1964), "two-cloud" and "tri-cloud" models, respectively. For the PFLs of 1989 August 17, the three "cloud" models are all applied alternately. The "two-cloud" and the "one-cloud" models have been extensively applied at the Yunnan Observatory (Gu et al. 1992, 1994, 1997; Li et al. 1993, 1994, 1998) and no longer have to be proved in the paper. But the "tri-cloud" model method, which is a special example of the MCM method, is first used here to deal with the "tri-peak" profiles. When $m = 3$, Eq. (1) becomes

$$\begin{aligned} I_\lambda = {} & S_1(1 - \mathrm{e}^{-\tau_{\lambda,1}}) + S_2(1 - \mathrm{e}^{-\tau_{\lambda,2}})\mathrm{e}^{-\tau_{\lambda,1}} \\ & + S_3(1 - \mathrm{e}^{-\tau_{\lambda,3}})\mathrm{e}^{-(\tau_{\lambda,1}+\tau_{\lambda,2})}. \end{aligned} \tag{10}$$

If $I_\lambda = F(\lambda, \boldsymbol{X})$, and $x_1, x_2, \ldots, x_{12}$ are $S_1, \tau_{0,1}, \Delta\lambda_{\mathrm{D},1}, \Delta\lambda_{0,1}$, $S_2, \tau_{0,2}, \Delta\lambda_{\mathrm{D},2}, \Delta\lambda_{0,2}$, $S_3, \tau_{0,3}$, $\Delta\lambda_{\mathrm{D},3}, \Delta\lambda_{0,3}$, then these twelve physical parameters can be derived.

It should be pointed out that different "cloud" models are utilized for different profiles: if a profile is single-peaked but asymmetric, or the profile is single-peaked and symmetric but its adjacent profiles in both sides are asymmetric, then, the two-cloud model is applied instead of the one-cloud model; if a profile is double-peaked, but its adjacent profiles are tri-peaked, and furthermore, the fitting results are not satisfactory with the "two-cloud model", then the "tri-cloud model" must be considered (Dun et al. 2000).

4. Derivation and computation of physical parameters

For each "cloud", the four parameters (S, $\Delta\lambda_\mathrm{D}$, τ_0 and $\Delta\lambda_0$) are obtained by fitting both profiles: the observed I_λ^{obs} and the theoretical one which is given by Eq. (1) at different sites of the PFLs. Some (profile) fitting results of four parameters and the calculation errors at five different sites of the PFLs are given in Fig. 2 and Table 1. Figure 2 shows that the theoretical profiles (shown with the dotted lines) are all in good agreement with those observed (shown with the solid lines) except for the line wings, showing good accuracy of the method. Hence, the parameters derived with the three "cloud model" methods can explain the observed profiles within a definite accuracy. So, the line-of-sight velocity $V_{//}$, column number density of hydrogen atoms at the second level along the line of sight N_2, excited temperature T_{ex} and microturblence velocity V_t may be calculated from the following relations (Tandberg-Hanssen 1995):

$$V_{//} = \frac{c}{\lambda_0}\Delta\lambda_0, \tag{11}$$

$$N_2 = \frac{m_\mathrm{e}c^2}{\sqrt{\pi}e^2\lambda_0^2 f_{2,4}}\tau_0\Delta\lambda_\mathrm{D}, \tag{12}$$

$$T_{\mathrm{ex}} = \frac{\frac{hc}{\lambda_0 k}}{\ln[(1 + \frac{2hc^2}{\lambda_0^5 S})\frac{b_4}{b_2}]} \tag{13}$$

and

$$V_\mathrm{t} \approx \sqrt{\frac{\Delta\lambda_\mathrm{D}^2 c^2}{\lambda_0^2} - \frac{2kT_{\mathrm{ex}}}{m_\mathrm{H}}}, \tag{14}$$

where both (the excited and kinematic) temperatures are assumed to be equal, $f_{2,4} = 0.1193$ is the oscillator strength of the H_β line, m_H the mean atomic mass of hydrogen, k is Boltzmann's constant, h is Planck's constant, m_e and e are the mass and charge of an electron, respectively, b_2 and b_4 are departure factors from LTE state and as an approximation, the state departure from LTE in the PFLs is assumed to be the same as that in a prominence which was given by Gouttebroze et al. (1993). Based on Eqs. (11)–(14), four physical quantities are calculated at different sites of the PFLs, the quantities at the five sites are listed in Table 2.

The electron density and gas pressure of the PFLs may be derived from the approximate computation of non-LTE. An approximate relation between the electron density n_e and the density of hydrogen atoms in a unit volume of the second level along the line of sight n_2 was proposed by Poland et al. (1971):

$n_\mathrm{e} \sim 3.2 \times 10^8\sqrt{n_2}$ and $N_2 = n_2 \times D$, where, D is the thickness of the loop system along the line-of-sight direction. Based on the Figs. 4–7, D is considered as the leg width of the loop system, that approximately measures 1∼1.5 $\times 10^4$ km. Then, if N_2 is taken as 0.8∼4.0 $\times 10^{13}$ cm^{-2}, one may find that $n_\mathrm{e} = 2\sim6 \times 10^{10}$ cm^{-3} and electron pressure $P_\mathrm{e} = n_\mathrm{e}kT_{\mathrm{ex}}$, from which, $p_\mathrm{e} = 0.04\sim0.12$ dyn cm^{-2} can be obtained when $T_{\mathrm{ex}} \sim 1.5 \times 10^4$ K.

5. 2D physical parameter fields

The data obtained during the first time interval (02:35–02:40 UT) are plotted in two directions: along the slit (4″ between two adjacent points) direction and the scan

Table 1. Physical parameters derived from the methods of "one-cloud", "two-cloud" and "tri-cloud" models.

Profile No.	S_1	S_2	S_3	τ_{01}	τ_{02}	τ_{03}	$\Delta\lambda_{D1}$ Å	$\Delta\lambda_{D2}$ Å	$\Delta\lambda_{D3}$ Å	$\Delta\lambda_{01}$ Å	$\Delta\lambda_{02}$ Å	$\Delta\lambda_{03}$ Å	rms ($\leq \times 10^{-2}$)	m
1(110/013)	0.77			1.13			0.39			-0.05			0.14	1
2(110/003)	0.31	0.44		1.47	1.22		0.70	0.33		-0.43	-0.15		0.22	2
3(114/007)	0.40	0.20		0.55	1.29		0.34	0.48		-0.91	-0.17		0.32	2
4(113/006)	0.49	0.45	0.42	0.49	0.46	0.44	0.37	0.34	0.30	-0.87	-0.31	0.25	0.28	3
5(113/007)	0.32	0.60	0.81	0.16	0.43	0.19	0.24	0.85	0.36	-0.92	-0.29	0.21	0.42	3

Table 2. Four physical quantities computed based on Eqs. (11)–(14) and Table 1.

Profile Number	cloud 1 $V_{//}$ km/s	V_t km/s	T_{ex} 10^4 K	N_2 10^{13} cm^{-2}	cloud 2 $V_{//}$ km/s	V_t km/s	T_{ex} 10^4 K	N_2 10^{13} cm^{-2}	cloud 3 $V_{//}$ km/s	V_t km/s	T_{ex} 10^4 K	N_2 10^{13} cm^{-2}
1(110/013)	- 0.39	21.81	0.63	3.12								
2(110/003)	-26.53	12.77	1.22	7.30	- 9.26	22.39	1.42	2.85				
3(114/007)	-56.15	19.60	1.36	1.33	-10.49	26.56	1.04	4.39				
4(113/006)	-53.68	16.53	1.49	1.28	-19.13	14.21	1.43	1.11	15.43	10.58	1.39	0.94
5(113/007)	-56.76	3.73	1.24	0.27	-17.89	49.77	1.65	2.59	12.96	12.94	1.96	0.48

($6''$ in a step distance) direction based on different positions of the PFLs, thereby obtaining their two-dimensional distributions in $V_{//}, N_2, T_{\rm ex}$ and $V_{\rm t}$, respectively (Figs. 4, 5, 6 and 7). These 2D distributions are useful for the study of the global properties of the PFLs.

Comparing 2D H_β spectrograms (Figs. 4–7) with the H_β filtergrams (Fig. 1c), one can see that there is little difference in morphology, because the latter shows higher spatial resolution (1–$2''$) than the former. Figures 4–7 and Fig. 1c all show that the PFLs may be considered as a whole loop system or an arcade-like structure, which possesses a number of sub-loops with different height and unequal legs.

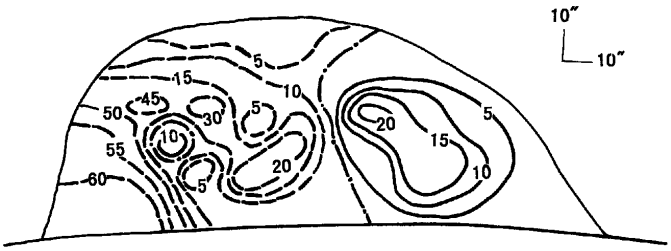

Fig. 4. The line-of-sight velocity fields observed from 02:35 UT to 02:40 UT on August 17, 1989 at the Yunnan Observatory. The solid lines refer to the red-shift velocity, the deashed lines refer to the blue-shift velocity, and the dashed-dotted lines show the zero velocity, with the unit of velocity being km s^{-1}. West is up, and south is to the right.

5.1. The line-of-sight velocity field $V_{//}$

The iso-velocity contour of $V_{//}$ is given in Fig. 4, a zero velocity line indicated with the dashed-dotted line runs down from the top of the loop system to its bottom and divides the loop system into two parts: the blue-shift velocity (moving towards the observer) in the north leg and the red-shift one (leaving the observer) in the south leg. The former is more predominant than the latter, with the blue-shift velocity increasing gradually along its leg from the top of the loop system downwards to the loop feet, where the maximum velocity reaches 60 km s^{-1}, and there are some maximum and minimum velocity "mounds" within the area of the north leg. For the red-shift velocity, there is a maximum velocity "mounds" of 20 km s^{-1} in the middle of the leg near the zero velocity line, the velocity then decreases gradually all aroud. In addtion, there is a small region with a red-shift velocity within the north leg.

The ascending motion of the two brightest tops of subloops (designated with "A" and "B" in Fig. 1c, respectively.) is also given in Table 3, with the ascending velocities decreasing gradually to less than 10 km s^{-1}, which is in agreement with the statistics given by Švestka (1996).

Table 3. Height variation and ascending motion for the tops of the two sub-loops which are indicated with "A" and "B" in Fig. 1c, respectively.

No.	1	2	3	4	5	6
Time (UT)	01:47:35	02:09:23	02:12:05	02:19:28	02:38:18	02:49:10
Δ t (s)		1308	162	443	1130	652
Height	5.60	8.70	9.95	11.19	15.54	18.28
(10^3 km)	11.19	20.52	21.76	23.13	26.11	26.86
Δ H		3.11	1.24	1.24	4.35	2.74
(10^3 km)		9.33	1.24	1.37	2.98	0.75
Ascending velocity		2.38	7.68	2.81	3.85	4.19
in average (km/s)		7.13	7.68	3.09	2.64	1.14

Note: The height and ascending velocity of "A" and "B" points are given in the first and the second lines, respectively.

5.2. Contour of the column number density N_2

An iso-density contour of N_2 along the line-of-sight direction is given in Fig. 5, which shows that the distribution of N_2 is inhomogeneous − there are some density "mounds" at the top and in the legs. In particular, two legs of the loop system are asymmetric in N_2, with N_2 being greater in the south leg (with an average value of 35×10^{12} cm^{-2}) than in the north leg (15×10^{12} cm^{-2} on average), which shows that the material in the south leg is much denser than that in the north one. Comparing Fig. 5 with Fig. 1c, one may find that the maximum value of N_2 in the south leg just corresponds to the brightest tops of two sub-loops A and B, and the N_2 "mound" may be related to the tops of other sub-loops. There is a secondary maximum region in the middle of the loop system, which runs along the axis of the loop system (i.e. the central line of the arcade). The variation in N_2 seems to have little relation to the height above the photosphere, similar to that seen in a prominence by Zhang et al. (1987). But it perhaps has some connection to the position within the arcade. In general, N_2 decreases from the central axis of the arcade to its periphery where the thickness D is small. The iso-value lines of N_2 show that there is a large gradient between the arcade axis and the boundary.

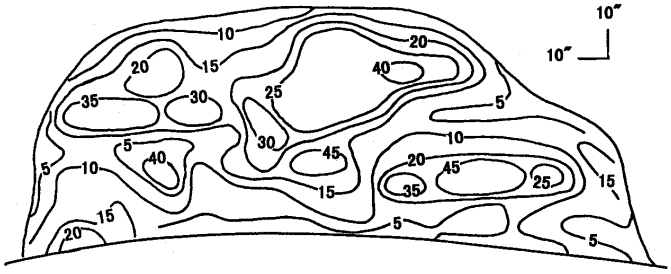

Fig. 5. Diagram of the column number density of hydrogen atoms at the second level along the line-of-sight direction, scaled by 10^{12} cm^{-2}. West is up, and south is to the right.

5.3. Distribution of the excited temperature T_{ex}

The temperature field of the loop system (Fig. 6) shows that T_{ex} in the south leg is much higher than that in the north leg indicating the temperature asymmetry. Iso-value lines of T_{ex} make an irregular arrangement, differing from that of the N_2 contour. On the whole, the temperature varies between 0.8 and 2.2×10^4 K and is lower at the top part than in the two legs. The highest value of T_{ex} is in the middle part of the south leg where it exceeds 2×10^4 K while the temperatures in the north leg and at the top are 1.2∼1.6 and 0.8∼1.2 $\times10^4$ K, respectively. No apparent relation between T_{ex} and the height above the photosphere has been found and no relation between T_{ex} and the position within the loop system (the arcade) has also been found. Comparing Fig. 5 with Fig. 6 carefully, it is found that T_{ex} and N_2 are opposite to each other in distribution, i.e. for some sites, T_{ex} is high, but N_2 is low and vice versa. It is easy to understand that the higher the temperature, the greater the number of hydrogen atoms which are excited to the fourth level (N_4). Thus, the number of atoms left in the second level N_2 decreases because of the conservation of the total atomic number.

5.4. Field of the turbulent velocity V_t

The distribution of V_t (Fig. 7) also denotes the asymmetry in both legs and an inhomogeneity for the whole loop system, but the difference between the south and north legs

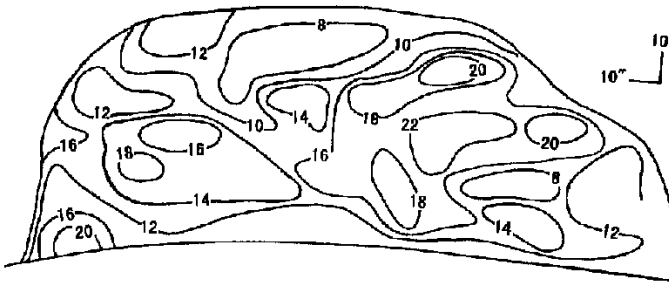

Fig. 6. Diagram of the excitation temperature scaled by 10^3 K. West is up, and south is to the right.

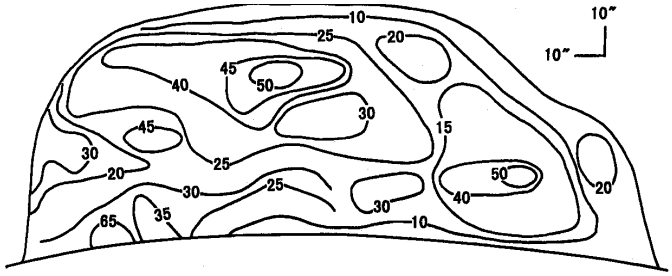

Fig. 7. Diagram of the micro-turbulence velocity, with the unit of velocity being $\mathrm{km\,s^{-1}}$. West is up, and south is to the right.

in V_t is smaller than that in N_2 and T_ex. V_t varies between 20∼50 $\mathrm{km\,s^{-1}}$, its maximum is located in the middle of the loop top, similar to N_2. The variation in V_t with position within the loop system is more apparent than that with height above the solar limb, V_t increases from the periphery of the loop system (the arcade) to the center axis of the arcade with a smaller gradient.

6. Discussion

It is found from computation that most of the profiles are suitable for the "two-cloud" model, a part of them (13%) for the "one-cloud" model and a few profiles (9.5%) for the "tri-cloud" model. Thus, the "two-cloud" model is the most useful method and its validity was tested by Heinzel et al. (1992) by comparing the results obtained by using the method and a full non-LTE method from the same flare of 1981 May 16. Fitting accuracy of the "tri-cloud" model is lower than that of the "two-cloud" and "one-cloud" models (ref. Table 1).

Because of the lower spatial resolution of the MW-SSHG data, one could not follow a fixed sub-loop. Hence, a definite sub-loop which is described by the same cloud number may be changed in other spectral frames, and it is difficult to draw 2D contours according to a fixed sub-loop. Therefore, Figs. 4–7 show, in fact, the average effect of many sub-loops. Different numbers of sub-loops superposed along the line-of-sight direction may be one of the direct causes of the existence of "mound" structures. For an MHD model, a thermal instability during the condensation process or an instability caused as a result of turbulence during the reconnection process could also result in the inhomogeneity in loops.

Based on the reconnection model of magnetic field lines, Forbes et al. (1989) predicted theoretically that the plasma densities of cool flare loops should be $\approx 10^{13}$ $\mathrm{cm^{-3}}$. Schmieder et al. (1995) studied the cool and hot PFLs of 1992 June 26, and estimated the electron density at 2.2×10^{10} $\mathrm{cm^{-3}}$. Gu et al. (1997) studied the PFLs of 1981 May 16 and estimated n_e to be between 2.5 and 5.6×10^{10} $\mathrm{cm^{-3}}$, P_e from 0.12 to 0.3 $\mathrm{dyn\,cm^{-2}}$ and V_t about 37.5 $\mathrm{km\,s^{-1}}$ when $T_\mathrm{e} = 15000$ K. Some parameters of PFLs are also derived from the NLTE radiative transfer diagnostics. The gas pressure of loops ranges between about 0.1 and 5 $\mathrm{dyn\,cm^{-2}}$ and the electron density between 10^{10} and 10^{12} $\mathrm{cm^{-3}}$ (Švestka 1987; Heinzel et al. 1992; Schmieder et al. 1995). The results given in this paper are all in accordance with those obtained by other authors mentioned above.

A comparison is made between the two PFLs obtained respectively on 1989 August 17 and 1984 February 18 (Li et al. 1993), with their 2D multi-parameter fields ($V_{//}$, N_2, T_ex and V_t) with H_β and H_α lines, being compared. The identical and different features are given as follows (comparing Figs. 4–7 with Fig. 7 and Figs. 10–12 of Li et al. 1993):

(1) For the N_2 distrubution, there is an asymmetry between the two legs and inhomogeneity ("mound" structure) in both PFLs, which may be formed by inequality between the two legs of sub-loops (ref. Fig. 1 of Li et al. 1993) due to overlapping between different numbers of sub-loops along the line-of-sight direction. N_2 of either PFLs is independent of the height above the photosphere, but is related to the site within a loop system.

(2) For both the PFLs, T_ex of either leg is asymmetric and inhomogenous. T_ex is higher in one leg than the other and the maximum of T_ex is not located at the top. Also, the variation of T_ex is between 8000 K and 20 000 K.

(3) It is a common feature for both systems that the maximum of V_t is located at the top part of the loop system. The average variation of V_t is between 15 and 45 $\mathrm{km\,s^{-1}}$.

(4) Although the maximum of $V_{//}$ is 60 $\mathrm{km\,s^{-1}}$ for the two systems, the patterns of $V_{//}$ are different from each other, because they are observed in different directions and perhaps have different models of material motion within the two systems. The former is almost in the front view and in the flash phase, at the opportune moment, the material within the loop system should mainly move upwards as a result of the "evaporation" of the chromospheric plasma, with the north leg showing the predominant blue-shift velocity. The latter is in the side view and in the gradual phase. At that time, most of the plasma matter falls down from its loop top, with the east leg showing red-shift velocity. Even in the same model of material motion, different morphologies of velocity fields will be obtained when the observation is made in different directions. For the flare of 1989 August 17, the velocity fields

observed at three different times were given by Dun et al. (2000) and Gu et al. (2000), showing a slow evolution (See Fig. 3 in Dun et al. (2000) or Fig. 1 in Gu et al. (2000)). It means that the velocity (or perhaps other parameters measured) will not cause essential differences in the development of the flare. Discussion of the temporal variations of the 2D distribution in N_2, $T_{\rm ex}$ and $V_{\rm t}$ will be given elsewhere.

(5) The electron density and pressure of the latter PFLs are higher than those of the former, which may be caused by different D in both PFLs.

PFLs are explained by some models of the reconnection of magnetic field lines in the high corona with an X-point where plasma is strongly heated. Forbes et al. (1989) considered that the slow shocks produced by the reconnection can generate a heat conduction front which propagates along the field lines to the chromosphere and ablates the chromospheric plasma, making it evaporate upwards, thereby forming the hot loops and flare ribbons. The matter coming from the chromosphere falls down along the post-flare-loops after the radiative cooling, and therefore, it can be expected that the hot material moves upwards (i.e. evaporation) and the cold moves downwards. In the impulsive phase, the evaporation would be the strongest and then it gradually weakens in the gradual phase when the matter within the loops mainly falls down. In the flash phase of flares, the energy deposited in the upper chromosphere heats the plasma to coronal temperatures and creates a region of high pressure which drives the hot plasma upwards. Thus, the blue-shifted velocity is observed for the flare on the solar disk in soft X-rays. In the underlying chromosphere, the plasma is driven downwards and is seen as the red-shifted H_α emission. Therefore, for a disk flare the blue-shift velocity usually disappears in the gradual phase. However, for a limb flare, if the angle between the normal line of the loop plane and the line of sight is not zero, then the matter in the loop moves up or down, as a result of the projection effect, the red-shift and blue-shift velocities may be observed at the same time, depending on the relative position between the loop plane and the observer.

Considering that the H_β spectral data of the PFLs on Aug. 17, 1989, were obtained during its maximum (02:40 UT), one suggestion is (Gu et al. 2000) that the matter in the PFLs should rise up from the loop foot to the loop top along the loop leg in a helical magnetic field line under the combined action of solar gravity, magnetic stress and the gradient of the atmospheric pressure in the loop system, and the material distribution in the PFLs would be inhomogeneous. In this case, a theoretical velocity field of the PFLs is approximately calculated with the aid of MHD theory. Results show the computed velocity field is basically similar to the observed one (02:35–02:40 UT). For the PFLs of 1984 February 18, which was observed during the gradual phase, a theoretical velocity field was given by Gu et al. (1989, 1991) under the assumption that plasma matter within the loop system should fall down from its top along a magnetic line of force within the loop leg, and calculations show that both of the velocity fields are well in accord.

7. Conclusions

The 2D H_β spectral data of the limb PFLs of 1989 August 17 are quantitatively studied in detail by means of the method of "multi-cloud model" (one-cloud, two-cloud and tri-cloud models) and the 2D distributions of four physical quantities (i.e. the line-of-sight velocity $V_{//}$, column number density of hydrogen atoms at the second level along the line-of-sight direction N_2, excitation temperature $T_{\rm ex}$ and micro-turblent velocity $V_{\rm t}$) are given in this paper. It is found that the velocities of blue shift on the north leg, where the maximum velocity of 60 $\rm km\,s^{-1}$ is reached are more predominant than those of the red-shift on the south leg. The values of N_2 and $T_{\rm ex}$ in the south leg are all much higher than those in the north leg. N_2 and $V_{\rm t}$ seem to change a little with the height above the photosphere, but they are related to the position within the whole loop system, decreasing from the center to the periphery. The maximum of N_2 is in the middle of the south leg, where the brightest two tops of sub-loops are located, and on average, $N_2 = 3.5 \times 10^{13}$ $\rm cm^{-2}$, $V_{\rm t} = 30 \sim 40$ $\rm km\,s^{-1}$. The maximum of $V_{\rm t}$ is located on the top part of the flare loop system, while $T_{\rm ex}$ on the top part is lower than that in the two legs. A higher temperature region is located in the middle of the south leg, being about $1.8\sim2.0 \times 10^4$ K on average. Electronic density $n_{\rm e}$ and pressure $P_{\rm e}$ are estimated to be $2\sim6 \times 10^{10}$ $\rm cm^{-3}$ and $0.04\sim0.12$ $\rm dyn\,cm^{-2}$, respectively.

The derived parameters are compared with those obtained from a limb flare loop system of 1984 February 18. Results show that most of the parameters and 2D distributions are similar for both flares except for the velocity fields which are observed in different directions and formed in different models of material motion within both PFLs. The asymmetry in the two loop legs and the inhomogeneity in the whole loop system are common features for both flares. This may be produced by the inequality between the two legs of sub-loops and the overlap of some sub-loops along the line of sight. In addition, the local thermal and turbulence instabilities during the condensation and the reconnection processes of magnetic field lines could cause the inhomogeneity within PFLs.

Acknowledgements. The authors thank the unknown referee very much for giving very useful comments and help. The authors are thankful to Dr. Ke-jun Li, Dr. Zhan-wen Han and Mr. Zhi-zhong Liu for their helps in preparing the manuscript and to Dr. Li Wei for providing very good H_β filtergrams.

References

Beckers, J. M. 1964, Ph.D. Thesis, Utrecht, AFCRL Env. Res. Papers, 49

Chen, J., & Lin, Y. Z. 1987, Acta Astroph. Sin., 7, 287

Dun, J. P., Gu, X. M., & Zhong, S. H. 2000, Ap&SS, 274, 473

Fang, C. 1985, Publ. of Nanjing University (Science), 21, 10

Forbes, T. G., & Malherbe, J. M. 1986, ApJ, 302, L67
Forbes, T. G., Malherbe, J. M., & Priest, E. R. 1989, Sol. Phys., 120, 285
Gouttebroze, P., Heinzel, P., & Vial, J. C. 1993, A&AS, 99, 513
Gu, X. M., Dun, J. P., & Zhong, S. H. 2000, Acta Astroph. Sin., 20, 414 (in English)
Gu, X. M., Lin, J., & Li, S. Q. 1991, Chin. J. of Space Sci., 11, 291
Gu, X. M., Lin, J., & Li, S. Q. 1989, Hvar Observatory Bull., vol. 13, 171
Gu, X. M., Lin, J., Luan, T., & Schmieder, B. 1992, A&A, 259, 649
Gu, X. M., Lin, J., Li, K. J., et al. 1994, A&A, 282, 240
Gu, X. M., Ding, Y. J., Luo, Z., & Schmieder, B. 1997, A&A, 324, 289
Gu, X. M., Lin, J., Li, K. J., & Dun, J. P. 1996, Ap&SS, 240, 263
Heinzel, P., Schmieder, B., Mein, P., et al. 1992, Sol. Phys., 139, 81
Kopp, R. A., & Pneumann, G. W. 1976, Sol. Phys., 50, 85
Li, K. J., Ding, Y. J., Bai, J. M., et al. 1994, Sol. Phys., 150, 87
Li, K. J., Ding, Y. J., Gu, X. M., et al. 1993, A&A, 269, 496
Li, K. J., B., Schmieder, J.-M., Malherbe, et al. 1998, Sol. Phys., 183, 323
Li, W. 1990, Pub. of Yunnan Obs., Special Issue III, 185
Poland, A., Skumanich, A., Athay, R. G., & Tandberg-Hanssen, E. 1971, Sol. Phys., 18, 391
Pneuman, G. W. 1981, in Solar Flare MHD, ed. E. R. Priest (Gordon and Breach. Sci. Pub.)
Schmieder, B., Heinzel, P., Wiik, J. E., et al. 1996a, Adv. Space Res., 17, 4/5, 111
Schmieder, B., Heinzel, P., Wiik, J. E., et al. 1995, Sol. Phys., 156, 337
Schmieder, B., Heinzel, P., van Driel-Gesztelyi, L., et al. 1996b,Sol. Phys., 165, 303
Švestka, Z. 1987, Sol. Phys., 108, 411
Švestka, Z. 1996, Sol. Phys., 169, 403
Sturrock, P. A. 1968, IAU Symp., 35, 471
Tandberg-Hanssen, E. 1995, The Nature of Solar Prominences (Kluwer Academic Publishers, Dordrecht, Holland), 19
Xuan, J. Y., & Lin, J. 1993, Sol. Phys., 144, 307
Ye, S. H., & Jin, J. H. 1985, Sol. Phys., 96, 113
Zhang, Q. Z., Livingston, W. C., Hu, J., & Fang, C. 1987, Sol. Phys., 114, 245